The Astrophysical Journal Letters, 797:L17 (7pp), 2014 December 20 doi:10.1088/2041-8205/797/2/L17

TRACING H_2 COLUMN DENSITY WITH ATOMIC CARBON (C I) AND CO ISOTOPOLOGS

N. Lo[1], M. R. Cunningham[2], P. A. Jones[2], L. Bronfman[1], P. C. Cortes[3], R. Simon[4], V. Lowe[2,5], L. Fissel[6], and G. Novak[6]
[1] Departamento de Astronomía, Universidad de Chile, Camino El Observatorio 1515, Las Condes, Santiago, Casilla 36-D, Chile
[2] School of Physics, University of New South Wales, Sydney, NSW 2052, Australia
[3] Joint ALMA Observatory, Santiago, Chile
[4] Physikalisches Institut, Universität zu Köln, Zülpicher Straße 77, 50937 Köln, Germany
[5] Australia Telescope National Facility, CSIRO Astronomy and Space Science, P.O. Box 76, Epping, NSW 1710, Australia
[6] Northwestern University, Center for Interdisciplinary Exploration and Research in Astrophysics (CIERA) and Department of Physics & Astronomy, 2145 Sheridan Road, Evanston, IL 60208, USA
Received 2014 August 23; accepted 2014 November 11; published 2014 December 3

ABSTRACT

We present the first results of neutral carbon ([C I] $^3P_1$–$^3P_0$ at 492 GHz) and carbon monoxide (^{13}CO, $J = 1$–0) mapping in the Vela Molecular Ridge cloud C (VMR-C) and the G333 giant molecular cloud complexes with the NANTEN2 and Mopra telescopes. For the four regions mapped in this work, we find that [C I] has very similar spectral emission profiles to ^{13}CO, with comparable line widths. We find that [C I] has an opacity of 0.1–1.3 across the mapped region while the [C I]/^{13}CO peak brightness temperature ratio is between 0.2 and 0.8. The [C I] column density is an order of magnitude lower than that of ^{13}CO. The H_2 column density derived from [C I] is comparable to values obtained from ^{12}CO. Our maps show that C I is preferentially detected in gas with low temperatures (below 20 K), which possibly explains the comparable H_2 column density calculated from both tracers (both C I and ^{12}CO underestimate column density), as a significant amount of the C I in the warmer gas is likely in the higher energy state transition ([C I] $^3P_2$–$^3P_1$ at 810 GHz), and thus it is likely that observations of both the above [C I] transitions are needed in order to recover the total H_2 column density.

Key words: ISM: atoms – ISM: clouds – ISM: molecules – stars: formation

Online-only material: color figures

1. INTRODUCTION

Carbon monoxide (CO) is often used as a tracer of H_2 density in molecular clouds, as it is abundant and easy to observe. However, it is known to be unreliable as it is optically thick in star forming regions (e.g., Shetty et al. 2011). With a new generation of telescopes capable of mapping at sub-millimeter wavelengths, there is a revival of interest in utilizing neutral atomic carbon as a tracer of molecular cloud column density, both observationally and in numerical simulations (see e.g., Shimajiri et al. 2013; Offner et al. 2014; Glover et al. 2014). One of the perceived advantages of atomic carbon (C I) over CO is that it continues to exist in regions of low dust extinction and strong radiation (commonly found in star forming regions), where CO suffers from photodissociation and turns into neutral carbon and oxygen. Here we investigate the effect that density and temperature have on H_2 column density calculated from [C I] and how it compares to that calculated from the CO isotopologs.

Of the four sources mapped here (see Table 1), three are in the G333 giant molecular cloud (GMC), located at a distance of 3.6 kpc, while NE-RCW36 is northeast of the RCW36 H II region in the Vela Molecular Ridge cloud C (VMR-C) at a distance of 700 pc. Both the G333 and VMR-C clouds have been extensively mapped at various wavelengths, including IR (Spitzer GLIMPSE and MIPSGAL, BLAST, Herschel), millimeter dust, and molecular lines (e.g., Yamaguchi et al. 1999; Mookerjea et al. 2004; Wong et al. 2008; Lo et al. 2009; Netterfield et al. 2009). From 1.2 mm dust continuum observations, the sources (clumps) in G333 have masses of $\sim 10^3\,M_\odot$ (Mookerjea et al. 2004), while the clumps in NE-RCW36 have an order of magnitude lower mass of $\sim 70\,M_\odot$ (Netterfield et al. 2009). Over the last two years, we have started a program to map these two clouds in atomic carbon emission with the NANTEN2 Telescope in Chile. We aim to investigate the distribution of C I in comparison to not only the CO isotopologs, but also various other chemical species such as N_2H^+, HNC, CS, and other dense gas tracers between 86 and 99 GHz.

We are currently completing the mapping of C I in G333 and the VMR-C, and here present our first result from the four mapped regions, focusing on the comparison between the C I and CO isotopologs. The selected regions are all associated with embedded stellar clusters and H II regions (see Table 1).

2. OBSERVATIONS AND DATA REDUCTION

The atomic carbon ([C I] ($^3P_1 - ^3P_0$) at 492.16 GHz, hereafter simply referred to as [C I]) observations presented in this Letter were carried out in 2013 with the NANTEN2 Telescope[7] at Pampa la Bola, Chile. The maps were collected with the 2×8 pixel array KOSMA SMART receiver and an eXtended bandwidth Fast Fourier Transfer Spectrometer (XFFTS) as backend, 2.5 GHz bandwidth, and 32768 channels. At 465 GHz, it has a FWHM beam size of ∼37 arcsec. Data were reduced with CLASS (GILDAS package), and have velocity resolution of 0.2 km s^{-1}.

The CO, ^{13}CO, and C^{18}O maps were collected with the Mopra Telescope from 2005 to 2007 for G333 and from 2012 to 2014 for VMR-C (for details, see Bains et al. 2006; Wong et al. 2008; Lo et al. 2009). At 3 mm wavelengths, the Mopra telescope has a FWHM beam size of ∼36 arcsec and velocity resolution of ∼0.1 km s^{-1} channel^{-1} at 100 GHz (Ladd et al. 2005). Data were reduced using the Livedata and Gridzilla

[7] http://www.astro.uni-koeln.de/nanten2/

Table 1
Observational and Physical Parameters of the Sources

	IRAS16164–5046[a]	IRAS16172–5028[b]	IRAS16177–5018[c]	NE-RCW36[d]
Pointing center[e] (α, δ)	16 22.17, −50 06.1	16 21.06, −50 35.38	16 21.54, −50 25.33	08 59.43, −43 43.87
Parent Complex	G333	G333	G333	VMR-C
Distance	3.6 kpc[f]	3.6 kpc[f]	3.6 kpc[f]	0.7 kpc[g]
rms chan^{-1} (NANTEN2/Mopra)	0.4/0.3 K	0.3/0.3 K	0.3/0.3 K	0.3/0.2 K
$V_{\rm C\,I}$ (km s^{-1})[h]	−47, −57	−45, −51, −54, −61	−45, −51, −58	4.2, 7.0
$V_{\rm ^{13}CO}$ (km s^{-1})[h]	−48, −57	−45, −51, −54, −61	−40, −43, −50, −56	4.2, 7.0
$\Delta V_{\rm C\,I}$ (km s^{-1})[h]	2.5, 5.9	1.7, 5.6, 6.2, 4.4	6.7, 6.0, 6.5	2.5, 2.7
$\Delta V_{\rm ^{13}CO}$ (km s^{-1})[h]	5.9, 5.6	2.8, 4.2, 6.2, 3.1	4.2, 3.1, 6.0, 6.8	1.5, 2.6
$\tau_{\rm C\,I}$[i]	0.2–1.3 (0.5)	0.2–0.8 (0.3)	0.1–0.6 (0.3)	0.1–0.8 (0.3)
$\tau_{\rm ^{13}CO}$[i]	0.9–5.3 (2.8)	0.1–5.3 (2.2)	0.1–4.3 (2.2)	0.04–3.0 (0.5)
$N_{\rm C\,I}$ ($\times10^{17}$ cm^{-2})[i]	0.2–7 (2.2)	0.9–8 (2.9)	0.1–6 (2.6)	0.1–3 (1.3)
$N_{\rm ^{13}CO}$ ($\times10^{17}$ cm^{-2})[i]	3–59 (9.6)	0.3–99 (19)	0.5–100 (28)	0.1–11 (0.8)
$T_{\rm ex}$ (K)[i]	8–16 (12)	14–29 (19)[i]	17–29 (21)	12–34 (19)
$N_{\rm H2-CO}$ ($\times10^{22}$ cm^{-2})[j]	0.5–2.2 (1.9)	2.4–6.6 (3.7)	2.8–5.6 (3.9)	0.7–2.1 (1.3)
$N_{\rm H2-C\,I}$ ($\times10^{22}$ cm^{-2})[j]	0.3–2.6 (0.8)	1.1–5.1 (1.8)	0.8–4.1 (1.6)	0.3–1.9 (0.9)

Notes.
[a] IRAS16164–5046: One of the most luminous far-infrared (FIR) sources in the Galaxy (Becklin et al. 1973); associated with the H II region G333.6-0.22, H_2O, and OH masers (Batchelor et al. 1980; Caswell 1998); harbors a young OB cluster (e.g., Fujiyoshi et al. 2006; Grave et al. 2014).
[b] IRAS16172-5028: Strongest source of SiO emission in G333 (Lo et al. 2007). Associated with the H II region G333.1-0.4, contains an embedded OB star cluster in very early evolutionary stages (Figueredo et al. 2005), and H_2O, OH, and CH_3OH masers (Breen et al. 2007; Caswell 1998; Caswell et al. 1995).
[c] IRAS16177–5018: Part of the H II region RCW106, contains the ultrahot star IRS1, likely an O3 I supergiant (Roman-Lopes et al. 2009).
[d] NE-RCW36: Associated with the RCW36 H II region, which contains a cluster of several hundred stars with the most massive star being a type O8 or O9 (see Minier et al. 2013, and references therein).
[e] The coordinates denote pointing centers for the maps (J2000).
[f] Lockman (1979).
[g] Murphy & May (1991).
[h] Velocity component (V) and line width (ΔV) obtained from Gaussian fits to the spectra in Figure 2.
[i] Opacity (τ), column density (N) of the C I and ^{13}CO maps, excitation temperature ($T_{\rm ex}$) derived from peak ^{12}CO emission.
[j] H_2 column density derived from ^{12}CO ($N_{\rm H2-CO}$) and C I ($N_{\rm H2-C\,I}$). Note that the ranges for j and k indicate the highest and lowest values across the maps of each of the sources (not per pixel), and median values are in brackets.

packages from the CSIRO/CASS. The Mopra data are gridded to the same spacing as the NANTEN2 [C I] data, which equates to 0.13 pc for RCW36 and 0.64 pc for the three G333 sources.

3. RESULTS

3.1. Spatial and Velocity Distributions

Integrated emission maps of ^{13}CO (contours) overlaid on [C I] (color) of the four sources are shown in Figure 1. Integrated velocity ranges are −70 to −52 km s^{-1} for IRAS16164–5046, −65 to −33 km s^{-1} for IRAS16172–5028 and IRAS16177–5018, and 2 to 12 km s^{-1} for NE-RCW36. There are two distinct velocity components in IRAS16164–5046 (Figure 2 spectra): −57 km s^{-1} is the main component while the −48 km s^{-1} component is due to a source southeast of IRAS16164–5046 and is outside the presented map. Hence, the intensity map and calculations that follow are based on emission integrated over the −57 km s^{-1} velocity component for this source.

In general, the bulk of [C I] emission for the three G333 sources has a similar distribution to the ^{13}CO emission, with its peak integrated emission also coinciding well with ^{13}CO, such as the ring structure seen in IRAS16177–5018 (Figure 1, bottom left). In contrast for NE-RCW36 (Figure 1, bottom right), there are two [C I] peaks; the northeast peak (RA = $9^{\rm h}59^{\rm m}32^{\rm s}$, Dec = $-43^{\rm d}43^{\rm m}50^{\rm s}$) does not have any corresponding ^{13}CO emission peak, and the southwest one (RA = $9^{\rm h}59^{\rm m}23^{\rm s}$, Dec = $-43^{\rm d}45^{\rm m}00^{\rm s}$) is offset from the ^{13}CO clump (contours).

To show the velocity structure of these regions, position–velocity (PV) diagrams of [C I] (grayscale) and ^{13}CO (contours) are plotted in Figure 2 (top row), with the line profiles of [C I] and ^{13}CO averaged over the region in the integrated emission maps (Figure 1, bottom four panels). [C I] and ^{13}CO have similar velocity structure, in the form of centroid velocity, line widths, and line wings/shoulders due to outflows and infall, as shown in the Gaussian-fitted parameters of the spectra (Table 1). As mentioned previously, the −48 km s^{-1} component of IRAS16164–5046 is due to a different source outside the presented map; here the PV diagram shows that this emission is detached from the main source. The NE-RCW36 PV diagram shows two separate velocity components, 4 and 7 km s^{-1}, which are also spatially separated. Since the column density calculation in this work is per spatial pixel, any spatially separable velocity structure does not affect the derivation of column density.

^{13}CO generally appears to be more extensive than [C I] as shown in Figure 1. However, we have determined that this is due the greater prevalence of artifacts in the [C I] maps, compared with those of the ^{13}CO maps. The noise in both the ^{13}CO and [C I] maps is non-Gaussian, and is influenced in particular by fluctuations in weather at the times maps were taken. For [C I] at the higher frequency of 492 GHz, the maps are more affected by poor weather than the ^{13}CO transition at 110 GHz. As the

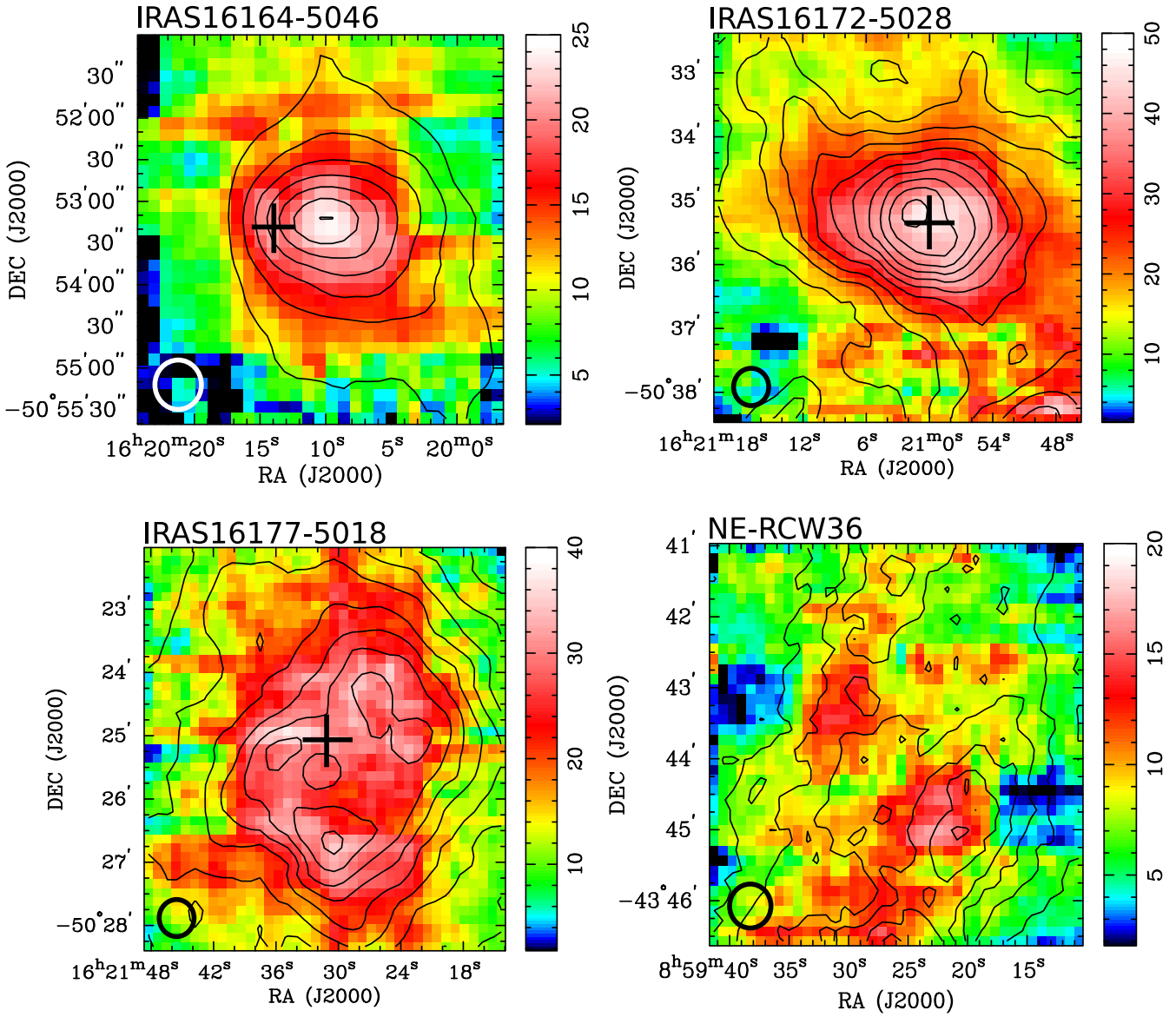

Figure 1. Integrated emission maps of ^{13}CO (contours) overlaid on [C I] of the four sources. The ^{13}CO contour levels start at 30% of the peak integrated emission, with increments of 10σ for NE-RCW36, and 20σ for the other three sources. The ^{13}CO peak integrated emission are 131, 189, 164, and 28 K km s^{-1} for IRAS16164–5046, IRAS16172–5028, IRAS16177–5018, and NE-RCW36, respectively. 1σ level ^{13}CO integrated emission maps are 0.7 K km s^{-1} for IRAS16164–5046, IRAS16172–5028, and IRAS16177–5018, 0.3 K km s^{-1} for NE-RCW36, and 3σ level maps are outside the presented ^{13}CO maps. Color scales are clipped at the 3σ level, where 1σ is 0.7 K km s^{-1} for IRAS16164–5046 and IRAS16172-5028, and 0.6 K km s^{-1} for IRAS16177-5018 and NE-RCW36. Beam sizes are marked by circles. The crosses mark the location of the *IRAS* sources, except RCW36, which is outside the map.

(A color version of this figure is available in the online journal.)

artifacts/noise are non-Gaussian, it has not been possible to determine a specific contour level of ^{13}CO, below which [C I] is no longer detected.

3.2. Column Densities

The column density maps presented in this work are derived per spatial pixel, utilizing the integrated intensity maps in Section 3.1. H_2 column density is obtained from the optically thick ^{12}CO, while C I and ^{13}CO column densities are corrected for opacity at each spatial pixel position.

For the H_2 column density, we utilize the empirical relation between H_2 and ^{12}CO for Galactic molecular clouds (Shetty et al. 2011),

$$N_{\rm H_2} = 2 \times 10^{20} \int T_{\rm MB}({\rm CO, J = 1 \rightarrow 0}) dV\,. \quad (1)$$

We follow the column density calculation outlined in Oka et al. (2001) for C I, which we repeat briefly here:

$$N_{\rm C\,I} = 1.98 \times 10^{15} \int T_{\rm MB} dV\; Q(T_{\rm ex}) e^{E_1/(kT_{\rm ex})} \times \left[1 - \frac{J_\nu(T_{\rm BB})}{J_\nu(T_{\rm ex})}\right]^{-1} \frac{\tau_{\rm C\,I}}{1 - e^{-\tau_{\rm C\,I}}}, \quad (2)$$

where $\int T_{\rm MB} dV$ is the integrated emission of [C I] and $Q(T_{\rm ex})$ is the partition function,

$$Q(T_{\rm ex}) = 1 + 3e^{E_1/(kT_{\rm ex})} + 5e^{E_2/(kT_{\rm ex})}, \quad (3)$$

with energy levels of $E_1/k = 23.6$ K and $E_2/k = 62.5$ K, $J_\nu(T_{\rm BB})$ and $J_\nu(T_{\rm ex})$ are the radiation temperature of cosmic

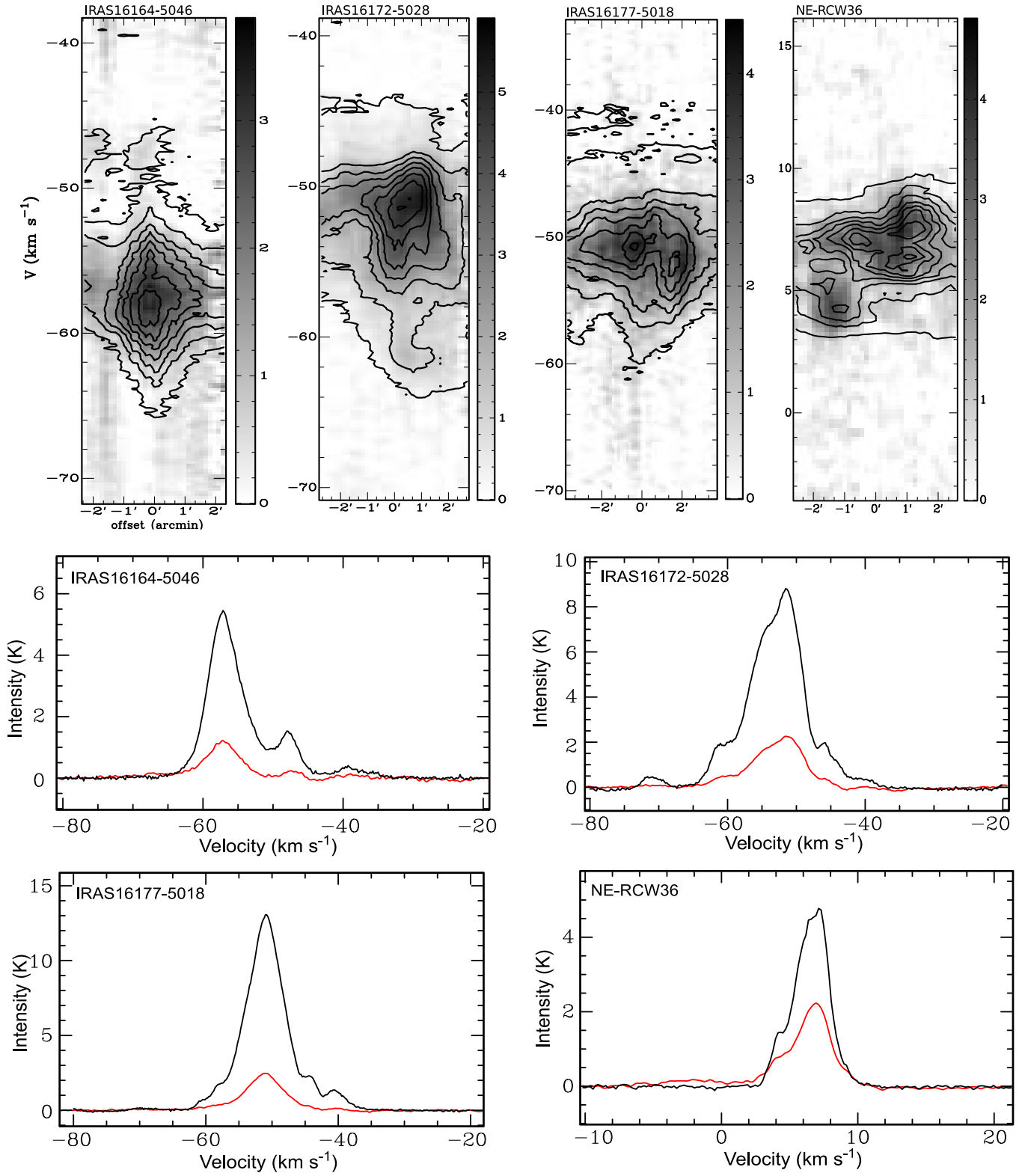

Figure 2. (Top row) [C I] and ^{13}CO (contours) position–velocity (PV). The contour levels start at the 5σ noise level with increment of 10σ, where 1σ is 0.2 K for IRAS16164–5046, 0.3 K for IRAS16172–5028 and IRAS16177–5018, and 0.1 K for NE-RCW36. PV cuts across each of the sources from NE to SW. (Line profiles) Averaged [C I] (red) and ^{13}CO (black) spectra over the area are shown in Figure 1.

(A color version of this figure is available in the online journal.)

background radiation ($T_{\rm BB} = 2.7$ K) and excitation temperature ($T_{\rm ex}$), respectively, and $\tau_{\rm C\,I}$ is the opacity,

$$\tau_{\rm C\,I} = -\ln\left\{1 - \frac{T_{\rm MB}}{\eta_f\,[J_\nu(T_{\rm ex}) - J_\nu(T_{\rm BB})]}\right\}, \quad (4)$$

where we assume the beam filling factor $\eta_f = 1$. Assuming C I has the same excitation temperature as the optically thick ^{12}CO at each of the spatial pixels, which is derived from the peak brightness temperature of ^{12}CO (Glover et al. 2014). We found that the opacity of C I is between 0.1 and 1.3 across the maps. The total column density of C I is between (0.1–8.4) $\times$ 10^{17} cm^{-2}, where IRAS16172–5028 has the highest peak column density of 8.4 $\times$ 10^{17} cm^{-2}, and NE-RCW36 has the lowest peak column density of 3.3 $\times$ 10^{17} cm^{-2}.

For the ^{13}CO column density, we corrected the ^{13}CO opacity by assuming that C^{18}O is optically thin, and taking an isotopolog ratio of $\tau_{\rm 13CO} = 7.4\tau_{\rm C18O}$ for the three sources in the G333 GMC (Wong et al. 2008), and 5.5 for NE-RCW36. The opacity is then obtained by solving the brightness temperature–opacity relation,

$$\frac{T_{\rm 13CO}}{T_{\rm C18O}} = \frac{1 - e^{-\tau_{\rm 13CO}}}{1 - e^{-\tau_{\rm C18O}}}. \quad (5)$$

Similar to C I, if we assume that ^{13}CO has the same excitation temperature as ^{12}CO, the total column density of ^{13}CO is then

$$N = \frac{8k\pi\nu^2}{hc^3 g_{\rm u} A_{\rm ul}} \frac{\tau}{1 - e^{-\tau}} e^{-E_u/(kT_{\rm ex})} Q(T_{\rm ex}) \int T_{\rm b} dV, \quad (6)$$

where $\int T_{\rm b} dV$ is the integrated emission of ^{13}CO, the upper energy level of $E_u/k = 5.3$ K, $A_{\rm ul}$ is the Einstein A coefficient in s^{-1}, transition frequency ν in Hz, the degeneracy g_u, and $Q(T_{\rm ex})$ is the partition function (Garden et al. 1991). We found the opacity of ^{13}CO to be between 0.1 and 5.3, and column density in the range of (0.1–100)$\times$$10^{17}$ cm^{-2}. IRAS16172–5028 and IRAS16177–5018 have the highest peak column densities ($\sim$$10^{19}$ cm^{-2}), while, similar to C I, NE-RCW36 has the lowest peak column density of 1.1 $\times$ 10^{18} cm^{-2}.

Simulation and modeling on how well C I traces molecular clouds suggest the $X_{\rm C\,I}$ factor has a value of 1.1×10^{21} cm^{-2} K^{-1} km^{-1} s, an analog to the widely used $X_{\rm CO}$ factor that connects the integrated ^{12}CO emission to H$_2$ column density (e.g., Offner et al. 2014; Glover et al. 2014). We apply this value to the integrated emission maps of [C I] to derive the H$_2$ column density ($N_{\rm H2-C\,I}$) and compare this to the H$_2$ column density maps we obtained from the ^{12}CO maps ($N_{\rm H2-CO}$). We note that the conversion factor is obtained from simulations and may not be fully applicable to the observed region here due to variables such as local abundance and chemical and physical conditions. We found that $N_{\rm H2-C\,I}$ traces 80% to 100% of $N_{\rm H2-CO}$ for regions where the ^{13}CO column density is between $\sim$5 and 7$\times$$10^{18}$ cm^{-2} and the C I column density is between $\sim$4 to 8 $\times$ 10^{17} cm^{-2} for the three G333 *IRAS* sources. For NE-RCW36, the region is at $\sim$1 $\times$ 10^{17} cm^{-2} for ^{13}CO and $\sim$2 to 3 $\times$ 10^{17} cm^{-2} for C I. A summary of the derived physical properties is available in Table 1.

4. DISCUSSION

Recent C I mapping of the northern part of the Orion-A GMC by Shimajiri et al. (2013) found an opacity of 0.1–0.75, similar to what we find (0.1–0.8) for three of our sources, with the exception of IRAS16164–5046, which reaches as high as 1.3 in optical depth at the [C I] emission peak. The highest C I column density in this work is of the order of $\sim$$10^{17}$ cm^{-2}, which is an order of magnitude lower than the peak value $\sim$$10^{18}$ cm^{-2} found in Orion-A. However, this could be due to effects such as resolution (i.e., beam filling factor less than 1). In fact, modeling with the radiative transfer code RADEX (Van der Tak et al. 2007) for gas temperature shows that 10^{18} cm^{-2} better fits our sources (discussion below).

We also find that the C I column density peak is offset from the peak H$_2$ column density when the excitation temperature (both quantities derived from the peak ^{12}CO emission; Section 3.2) at the H$_2$ peak column density exceeds 25 K (Figure 3). This is unlikely to be due to the optical thickness of ^{12}CO "shifting" the apparent peak position, as from a cross check with the dust cores from ATLASGAL (Csengeri et al. 2014) and BLAST (Netterfield et al. 2009) data, their positions coincide well with the ^{12}CO peaks. Thus, the H$_2$ column density peaks, except for the source IRAS16177–5018, in which ^{12}CO is blended over various dust cores. In fact, at the peak C I column density position, $T_{\rm ex}$ is within 15 to 20 K. The only source (IRAS16164–5046) that has both the C I and H$_2$ column density peaks coincide has an excitation temperature of $\sim$15 K at this position. Furthermore, if we double the excitation temperature (>30 K) in C I column density calculations, it yields a lower column density at the C I peak position. Modeling of C I by Glover et al. (2014) shows that around 80% of C I is found in regions with temperature below 30 K, and, from our observations, we also find that C I is concentrated at places with lower excitation temperature (15 to 20 K). Depending on optical thickness, excitation temperature does not necessary equal gas kinetic temperature, and in the low opacity case, molecules are generally sub-thermally excited which makes the excitation temperature lower than kinetic temperature, so in either case, C I is found mainly in low-temperature gas. One possible explanation for this is that the C I data presented here is from the observations of lower fine structure transition at 492 GHz with an energy level of 23 K. As the gas temperature rises, more of the neutral carbon atoms populate the higher transition level at 810 GHz with an energy level of 62 K. To check whether this explanation is possible, we utilize the radiative transfer code RADEX by inputting gas temperatures in the range of 15–40 K. We find that as temperature rises, the intensity (population) of the 810 GHz transition increases from 2.8 to 20 K. Furthermore, the H$_2$ column density we obtained with C I is comparable to the H$_2$ column density derived from ^{12}CO, and ^{12}CO is an unreliable tracer at high density as it becomes optically thick (e.g., Shetty et al. 2011), and thus underestimates the column density. Despite that, the comparable H$_2$ column density suggests that a portion of the neutral carbon atoms in the $^3P_1$–$^3P_0$ state appear to be missing. If this is the case, and if a substantial amount of atomic carbon is in an energy state above the ground state, we should see a position offset of the 810 GHz [C I] transition for the sources here, and follow up observations in the future will further investigate this. More importantly, observations of both [C I] transitions maybe necessary to recover the total C I gas.

One possible uncertainty in our column density calculation comes from the velocity range in the integrated intensity maps. As shown in Section 3.1, these sources are not quiescent gases, they are turbulent with outflows (line wings). In order to access the effect of integrating over different gas components on column density derivation, two sets of velocity range are

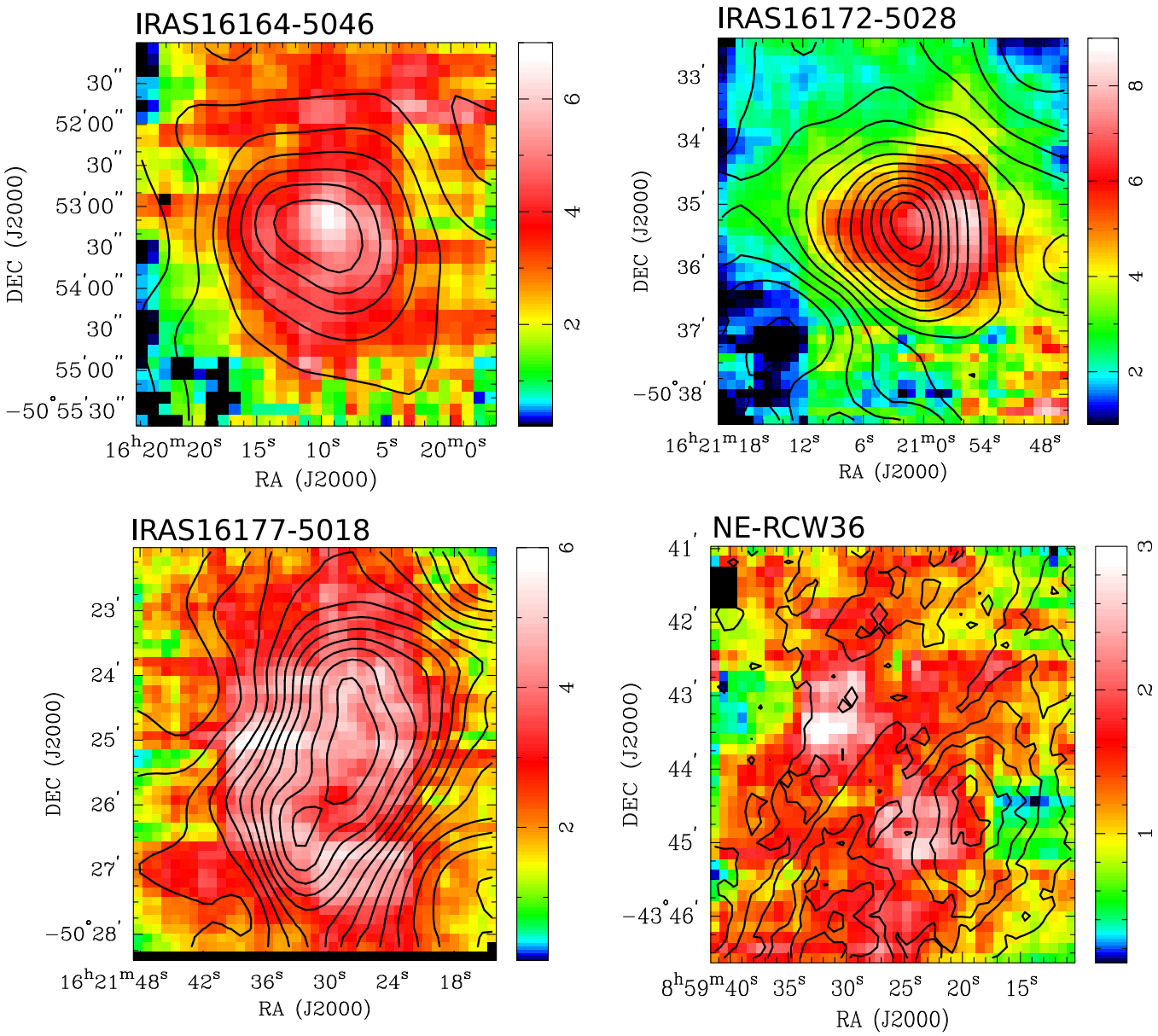

Figure 3. H_2 column density map (contours) overlaid on C I column density map (color) of the four sources. The column density maps are on scale of 10^{21} cm^{-2} and 10^{17} cm^{-2} for H_2 and C I. The H_2 contour levels start at 40% of peak column density (Table 1), except for IRAS16177–5018, which starts at 50%, the lowest visible contour level in the presented map. Contour steps are at 20σ, where 1σ is 1×10^{20} cm^{-2} for IRAS16164–5046, IRAS16177–5018, and NE-RCW36, and 1.5×10^{20} for IRAS16172-5028.

(A color version of this figure is available in the online journal.)

used: (1) integration over a velocity range that includes line wings/shoulders, (2) integration over the line width of the main core velocity component. In method (1), the H_2 column density derived from [C I] is comparable to those derived from ^{12}CO (Table 1). With method (2), H_2 column density obtained from [C I] is approximately 10% to 30% higher than those from ^{12}CO, but still within an order of magnitude. However, by integrating over the line width only can be problematic with ^{12}CO, as it is self-absorbed at the core velocity component, and the application of X factor requires ^{12}CO to be optically thick and integrated over the emission range. Given the H_2 column density derived from ^{12}CO and [C I] in both methods are comparable and within the same order of magnitude, the choice of velocity range does not alter the conclusion in this work.

Another uncertainty in deriving the H_2 column density is the value of the $X_{\rm C\,I}$ factor; unlike CO, the relationship between [C I] intensity and H_2 column density is not well studied. The value we used in this work is from simulation studies (Offner et al. 2014; Glover et al. 2014), not specifically calibrated for the regions presented. The simulations do not take into account active star formation, where strong UV radiation increases the abundance of C I, and thus altering the value of the $X_{\rm C\,I}$ factor. There is no observational/simulation study on the $X_{\rm C\,I}$ factor among active star forming regions (at the time of this work), but if star formation raises the abundance of C I, then the $X_{\rm C\,I}$ factor would be higher in these cases, and thus increase the derived H_2 column density. We are in the process of completing the C I mapping, along with various molecular lines at 3 mm wavelengths, we can calibrate the X factor of C I and

other molecules (e.g., HCO^+, CS, HCN) by comparing the H_2 density estimated from the spectral-energy-distribution fits of continuum emission.

5. CONCLUSION

We present the first results of C I mapping of the VMR-C and G333 GMCs, comparing the column density of H_2 derived from both the C I and CO isotopologs. The [C I] emission profile is similar to ^{13}CO with comparable line widths. We found that C I has an opacity between 0.1 to 1.3 and a column density of (0.1–8) $\times$ 10^{17} cm^{-2}, an order of magnitude lower than ^{13}CO column density. Utilizing the $X_{\rm C\,I}$ factor, we found an H_2 column density of the order of $\sim 10^{22}$ cm^{-2}, which is within the same order of magnitude of H_2 column density derived from ^{12}CO, and near 100% at the [C I] peak emission location. [C I] emission tends to peak at regions with low gas temperature ($<$20 K), and it yields the same H_2 column density as those derived from ^{12}CO at this temperature range. This could be caused because some of the carbon atoms are in a higher excitation state, though further mapping of the C I transition at 810 GHz will help confirm this.

Our results suggest that if the gas is warm (above 25 K), it is recommended to observe both of the [C I] transitions for a more accurate determination of H_2 column density. C I has the advantage of low opacity compared to ^{12}CO, while in low-density and low-extinction regions CO is dissociated into neutral carbon and oxygen, making C I a better tracer in these cases. However, in regions of dense gas where local abundance of ^{13}CO is known, ^{13}CO may be a better choice for probing H_2 column density, as it is easily observed due to the lower frequency of its emission lines.

N.L.'s postdoctoral fellowship is supported by CONICYT/FONDECYT postdoctorado, under project No. 3130540. L.B. acknowledges support by CONICYT Project PFB06. NANTEN2 Observatory is a collaboration between the Nagoya University, Osaka University, KOSMA, Universität zu Köln, Argelander-Institet Universität Bonn, Seoul National University, ETH Zürich, University of New South Wales, and Universidad de Chile. The Mopra Telescope is part of the Australia Telescope and was funded by the Commonwealth of Australia for operation as a national facility managed by CSIRO until 2012.

Facilities: Mopra, NANTEN2.

REFERENCES

Bains, I., Wong, T., Cunningham, M. R., et al. 2006, MNRAS, 367, 1609
Batchelor, R. A., Caswell, J. L., Haynes, R. F., et al. 1980, AuJPh, 33, 139
Becklin, E. E., Frogel, J. A., Neugebauer, G., et al. 1973, ApJL, 182, L125
Breen, S. L., Ellingsen, S. P., Johnston-Hollitt, M., et al. 2007, MNRAS, 377, 491
Caswell, J. L. 1998, MNRAS, 297, 215
Caswell, J. L., Vaile, R. A., Ellingsen, S. P., et al. 1995, MNRAS, 272, 96
Csengeri, T., Urquhart, J. S., Schuller, F., et al. 2014, A&A, 565, 75
Figuerêdo, E., Blum, R. D., Damineli, A., et al. 2005, AJ, 129, 1523
Fujiyoshi, T., Smith, C. H., Caswell, J. L., et al. 2006, MNRAS, 368, 1843
Garden, R. P., Hayashi, M., Hasegawa, T., et al. 1991, ApJ, 374, 540
Glover, S. C. O., Clark, P. C., Micic, M., & Molina, F. 2014, MNRAS, submitted, arXiv:1403.3530
Grave, J. M. C., Kumar, M. S. N., Ojha, D. K., et al. 2014, A&A, 563, AA123
Ladd, N., Purcell, C., Wong, T., & Robertson, S. 2005, PASA, 22, 62
Lo, N., Cunningham, M., Bains, I., et al. 2007, MNRAS, 381, L30
Lo, N., Cunningham, M. R., Jones, P. A., et al. 2009, MNRAS, 395, 1021
Lockman, F. J. 1979, ApJ, 232, 761
Minier, V., Tremblin, P., Hill, T., et al. 2013, A&A, 550, AA50
Mookerjea, B., Kramer, C., Nielbock, M., & Nyman, L.-Å. 2004, A&A, 426, 119
Murphy, D. C., & May, J. 1991, A&A, 247, 202
Netterfield, C. B., Ade, P. A. R., & Bock, J. J. 2009, ApJ, 707, 1824
Offner, S. S. R., Bisbas, T. G., Bell, T. A., & Viti, S. 2014, MNRAS, 440, 81
Oka, T., Yamamoto, S., Iwata, M., et al. 2001, ApJ, 558, 176
Roman-Lopes, A., Abraham, Z., Ortiz, R., & Rodriguez-Ardila, A. 2009, MNRAS, 394, 467
Shetty, R., Glover, S. C., Dullemond, C. P., & Klessen, R. S. 2011, MNRAS, 412, 1686
Shimajiri, Y., Sakai, T., Tsukagoshi, T., et al. 2013, ApJL, 774, L20
Van der Tak, F. F.S., Black, J. H., Schier, F. L., Jansen, D. J., & van Dishoeck, E. F. 2007, A&A, 468, 627
Wong, T., Ladd, E. F., Brisbin, D., et al. 2008, MNRAS, 386, 1069
Yamaguchi, N., Mizuno, N., Saito, H., et al. 1999, PASJ, 51, 775